

AD 608638

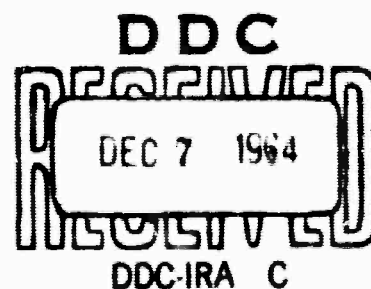
**Measurement of Fluid Properties for  
Magnetoplasmadynamic Power Generators  
Sixth Quarterly Technical Summary Report  
1 August -- 31 October 1964)**

**Contract No. Nonr-4104(00) and Amendment 1  
Order No.: ARPA 420      Project Code No. 3980**

**Engineering Department Report No. 4037**

34-P

COPY	2	OF	3	Jmc
HARD COPY			\$.	2.00
MICROFICHE			\$.	0.50



**Allison Division • General Motors**

**Indianapolis, Indiana**

**ARCHIVE COPY**

**BEST  
AVAILABLE COPY**

**Measurement of Fluid Properties for  
Magnetoplasma Dynamic Power Generators  
Sixth Quarterly Technical Summary Report  
1 August — 31 October 1964)**

**Contract No. Nonr-4104(00) and Amendment 1**  
**Order No.: ARPA 420                      Project Code No. 3980**

**Engineering Department Report No. 4037**


**17 November 1964**

**Written By:**



**R. T. Schneider,  
Program Manager**

**Approved:**



**F. G. Myers  
Research Director**

---

## FOREWORD

This technical summary report was prepared by the Research Department of the Allison Division of General Motors Corporation. The work reported was accomplished under Contract Nonr-4104(00) and Amendment No. 1 thereto.

The program was sponsored by the Advanced Research and Project Agency through the Power Branch of the Office of Naval Research under the direction of ARPA and Mr. J. A. Satkowski of ONR.

Allison personnel who contributed material for this report are:

H. E. Wilhelm  
R. O. Whitaker  
R. L. Koch

## TABLE OF CONTENTS

<u>Section</u>	<u>Title</u>	<u>Page</u>
I	Introduction . . . . .	1
II	Summary of Work Accomplished . . . . .	3
	Construction of Closed Loop Device . . . . .	3
	Test Runs . . . . .	3
	Theoretical Investigations . . . . .	4
III	Experimental Results . . . . .	5
	Runs with Pure Helium . . . . .	5
	Experimental Technique . . . . .	5
	Data with Pure Helium . . . . .	8
	Runs with Helium Seeded with Cesium . . . . .	11
	Voltage-Current Curves . . . . .	11
	Spectroscopic Observations. . . . .	15
IV	Theoretical Investigation . . . . .	21
	Calculation of Intercomponent Nonequilibrium in a Magnetoplasma- dynamic Converter . . . . .	21
	Converter Model . . . . .	21
	Plasma Equations . . . . .	21
	Initial Flow Data . . . . .	22
	Results and Discussion. . . . .	23
	Further Investigation. . . . .	26
	On the Nonobservability of the Full Open Faraday Load Voltage . . . . .	26
V	Conclusions . . . . .	29

## LIST OF ILLUSTRATIONS

<u>Figure</u>	<u>Title</u>	<u>Page</u>
1	Segmented electrodes . . . . .	5
2	Magnet current--field strength calibration curve. . . . .	6
3	Instrumentation for field strength recording . . . . .	7
4	Voltage output recording with 500-ohm load . . . . .	8
5	Voltage output recording with 1000-ohm load. . . . .	8
6	Voltage output recording with 5000-ohm load. . . . .	9
7	Voltage output recording with 20,000-ohm load. . . . .	10
8	Voltage output recording without load. . . . .	10
9	Voltage-current curves for cesium-seeded helium. . . . .	12
10	Voltage output curves obtained with segmented electrodes. . . . .	14
11	Spectrum photograph showing reversal of the cesium resonance line. . . . .	17
12	Densitometer traces showing reversal of the cesium resonance lines. . . . .	19
13	MPD converter cross section model . . . . .	21
14	Results of numerical integration . . . . .	24

## LIST OF TABLES

<u>Table</u>	<u>Title</u>	<u>Page</u>
1	Elementary particle constants. . . . .	22
II	Initial flow values . . . . .	22
III	Electrical flow quantities . . . . .	26

---

## I. INTRODUCTION

This report describes the progress achieved on Contract ONR Nonr-4104(00) from 1 August through 31 October. During this period sufficient operation experience was gained and design information was accumulated to justify building a large MPD test section. This new test section should deliver a nominal amount of power.

The Allison MPD system is now sufficiently refined that reliable operation can be ensured for an extended time. The next quarterly report will describe the design of the new test section. Details of voltage-current characteristics and saturation curves are included herein.

## II. SUMMARY OF WORK ACCOMPLISHED

### CONSTRUCTION OF CLOSED LOOP DEVICE

Minor design modifications in the closed loop system were made during the reporting period. The helium-cesium separation system was improved so that it is now possible to recover a large percentage of the cesium.

The seed injection system has also been improved so that a controllable cesium mass flow without fluctuations can be established and maintained for an extended time.

The design and construction of the new test section with a channel length of 50 cm was continued.

### TEST RUNS

Several helium-cesium runs were made. Voltage-current curves for different magnetic fields were plotted directly with x-y recorders. A family of curves with the magnetic field as a parameter was thus obtained. The voltage-current curves are straight lines. The magnetic field causes the voltage-current curves to rotate around one point at the current axis, as is expected from theory. Direct plotting of the voltage-current curves ensures that the curves are straight lines and have no occasional dips which could be overlooked in the interpolation when composing curves from different runs.

For the same reason, efforts were made to record the voltage output curves versus magnetic field directly from the generator to x-y plotters. In this case the load resistor was the parameter. Since it is not possible to measure the magnetic field directly during the run, the current through the magnet coils was monitored and this value was converted with a calibration curve into the corresponding value for magnetic field. For a direct plot, this transformation must be done continuously. Therefore, the signal from the magnet current shunt was sent via telephone lines to the computing center where an analog computer converted it to a signal corresponding to the magnetic field. This signal was then fed back into the x-y plotter.

Different spectroscopic measurements were also made and a few impurities were detected. The essential result of the spectroscopic observations, however, is that the electron temperature was equal to the gas temperature within the accuracy of measurement.



## THEORETICAL INVESTIGATIONS

A theory of the intercomponent thermal nonequilibrium was developed at small Hall coefficients including nonuniformities of the plasma and the thermal diffusion effect.

First numerical results for the buildup of the electron temperature nonequilibrium were obtained using the usual approximation which disregards the thermal diffusion effect. The numerical value of the buildup length is in good agreement with the approximate analytical formula obtained earlier.

### III. EXPERIMENTAL RESULTS

#### RUNS WITH PURE HELIUM

A previous report\* discussed MPD runs made with a working fluid of pure helium with no seed. Observations made during runs of that type are reported herein.

#### Experimental Technique

In the original run, one of the electrodes (the cathode) was a single plate, while the other electrode (the anode) consisted of pins.<sup>†</sup> In the present setup, segmented electrodes were used and only the high-voltage electrodes were pins. Figure 1 shows the electrodes.

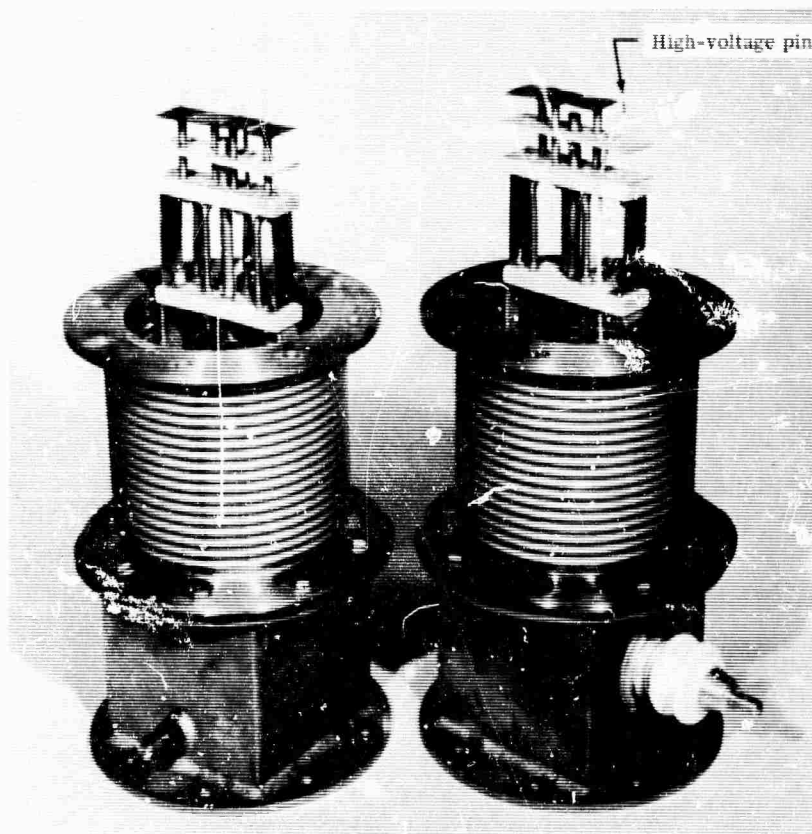


Figure 1. Segmented electrodes.

\*Measurement of Fluid Properties for Magnetoplasmadynamic Power Generators—Fourth Quarterly Technical Summary Report (1 February—30 April 1964), Indianapolis, Indiana, Allison Division, GMC, EDR 3861, 18 May 1964, pp 5-9.

<sup>†</sup>Ibid., Figure 1.

Segmented electrodes were used to prevent the cathode spot from moving downstream as had happened in previous experiments.\* With an arrested cathode spot as is achieved with the pin electrodes, it is much easier to judge how far downstream the induced conductivity can be extended. It should also be noted that with the high-voltage pin electrode, the electron emitting surface is several orders of magnitude smaller than previously and the area is more precisely defined.

During system operation, it is very desirable to monitor the magnetic field strength in the test section. However, no transducers are available which can be positioned in the test section and can endure the environment. The most practical alternative, then, is to measure magnet current. The calibration curve shown in Figure 2, may then be used to obtain field strength. To avoid the necessity of hand reducing data, the instrumentation setup of Figure 3 was employed.

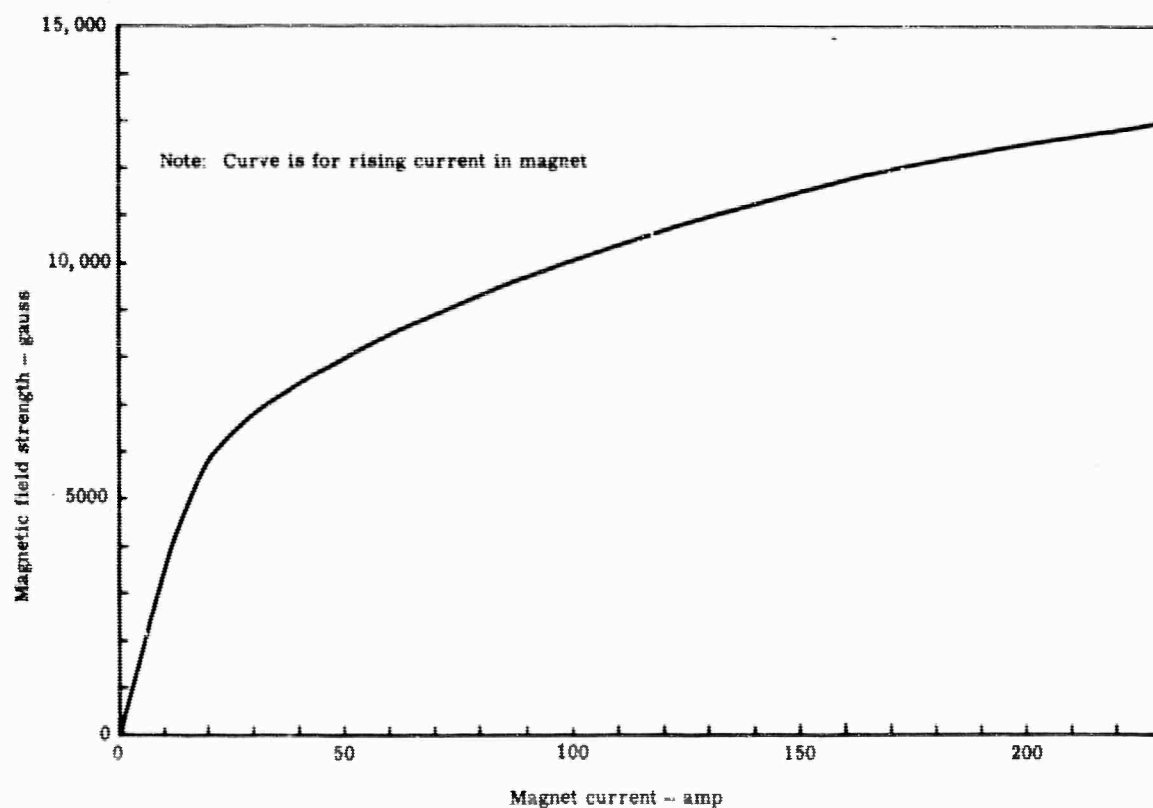


Figure 2. Magnet current--field strength calibration curve.

---

\*ibid., Figure 5.

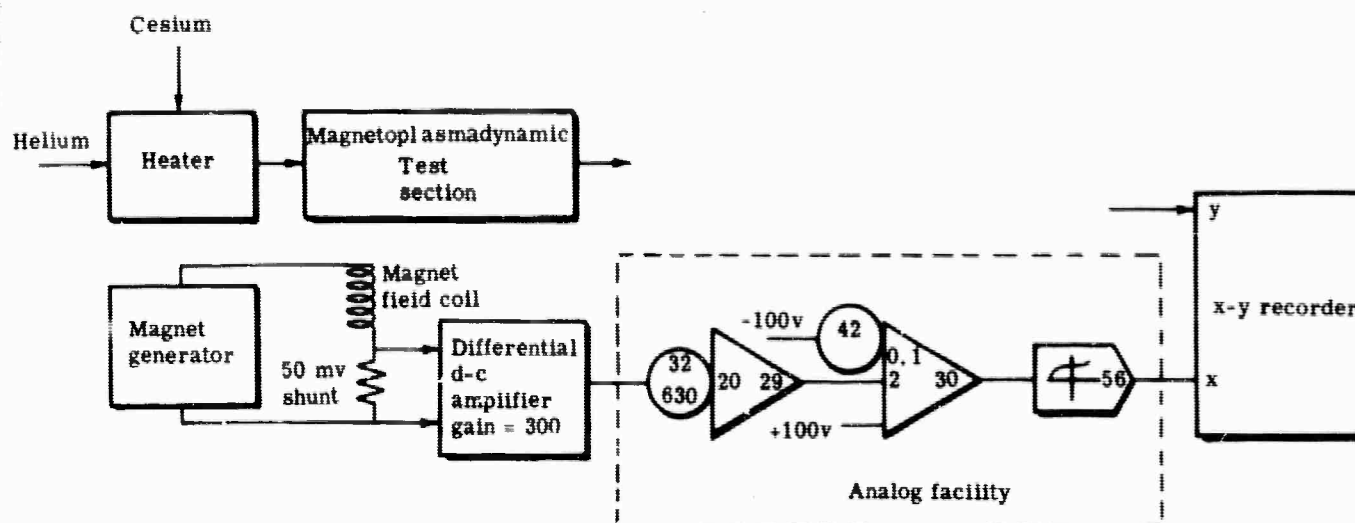


Figure 3. Instrumentation for field strength recording.

Magnet current passing through the 50-mv shunt developed a voltage which was amplified by the differential d-c amplifier.\* This amplifier is a chopper-stabilized unit of very low drift and very constant gain.

A specially installed cable delivered the output of the amplifier to the Allison analog computer facility—indicated by the portion of Figure 3 within the dotted perimeter.

The gain of the differential d-c amplifier was adjusted so that 300 amp flowing through the 50-mv shunt caused the output of amplifier 29 to change from 0 to 100 v. Amplifier 29 provided further gain. Potentiometer 42 (associated with amplifier 30) compensated for any slight zero drift in the differential d-c amplifier. The +100-v input and the gain of 2 applied to the main signal provided proper scaling for the function generator 56. Function generator 56 carried the magnetic field strength vs current curve of Figure 2. The output of the function generator was thus a voltage proportional to magnetic field.

The output of function generator 56 was returned via cable to the MPD laboratory and delivered to the x-axis of an x-y recorder. This permitted variables to be plotted directly as functions of magnetic field.

\*Kin-Tel Model 114C d-c amplifier and Model 191A rack module.

It is noted that the magnet used exhibited substantial hysteresis. The curve set up on the function generator was that for rising magnetization. Proper operation of the instrumentation required that before each test the magnet excitation be reduced to zero. Magnet current was then raised to approximately the test value and held for the duration of the test.

## Data with Pure Helium

Figures 4, 5, 6, 7, and 8 represent the raw data obtained from low-temperature runs with helium without seeding. The output voltage measured across a load resistor was plotted directly as a function of magnetic field. The load resistance appeared as a parameter. These curves are presented here because a saturation effect was observed. If the suspected reason for this effect is substantiated by further tests, it will be described in the final report. At that time, runs will also have been made using the large test section being constructed at the present time.

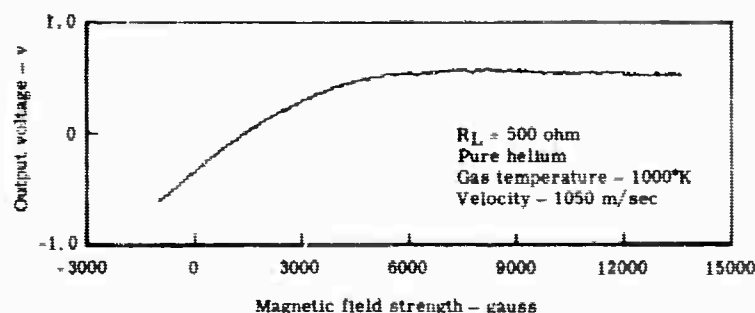


Figure 4. Voltage output recording with 500-ohm load.

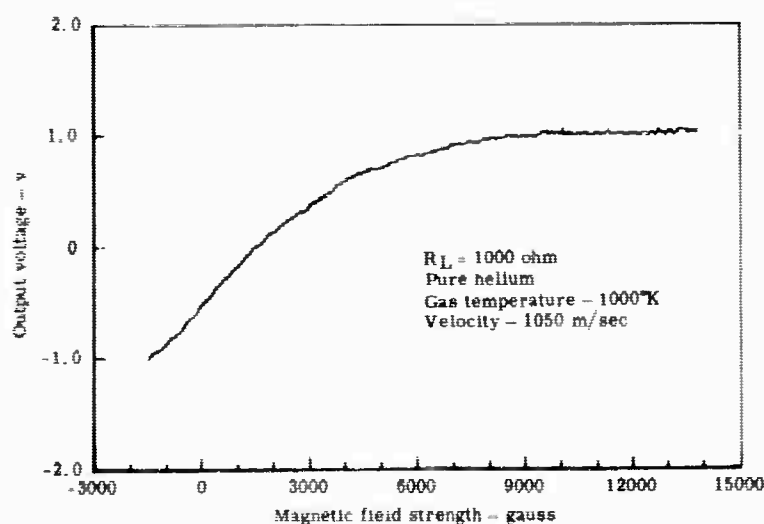


Figure 5. Voltage output recording with 1000-ohm load.

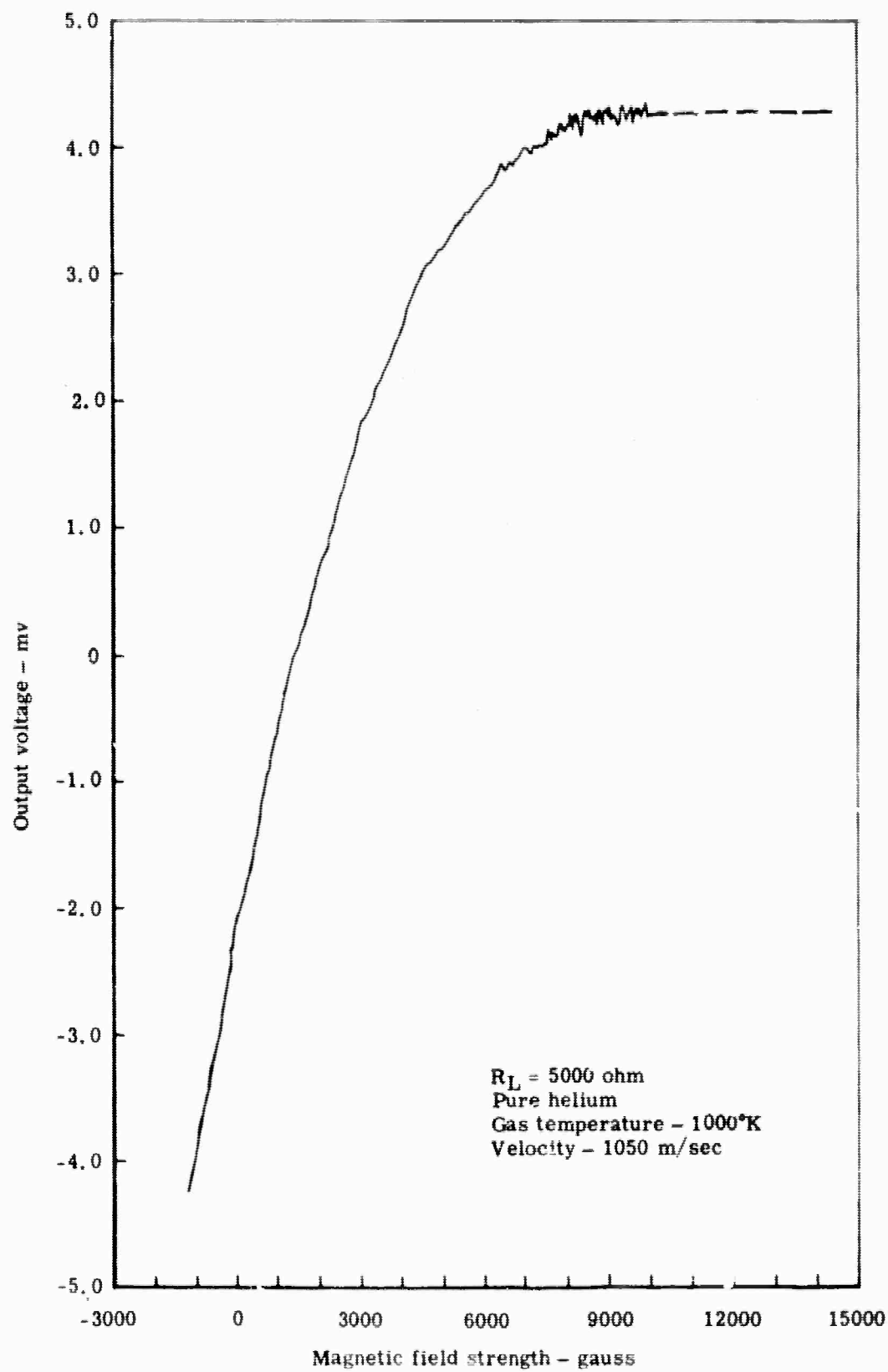


Figure 6. Voltage output recording with 5000-ohm load.

Figure 7. Voltage output recording with 20,000-ohm load.

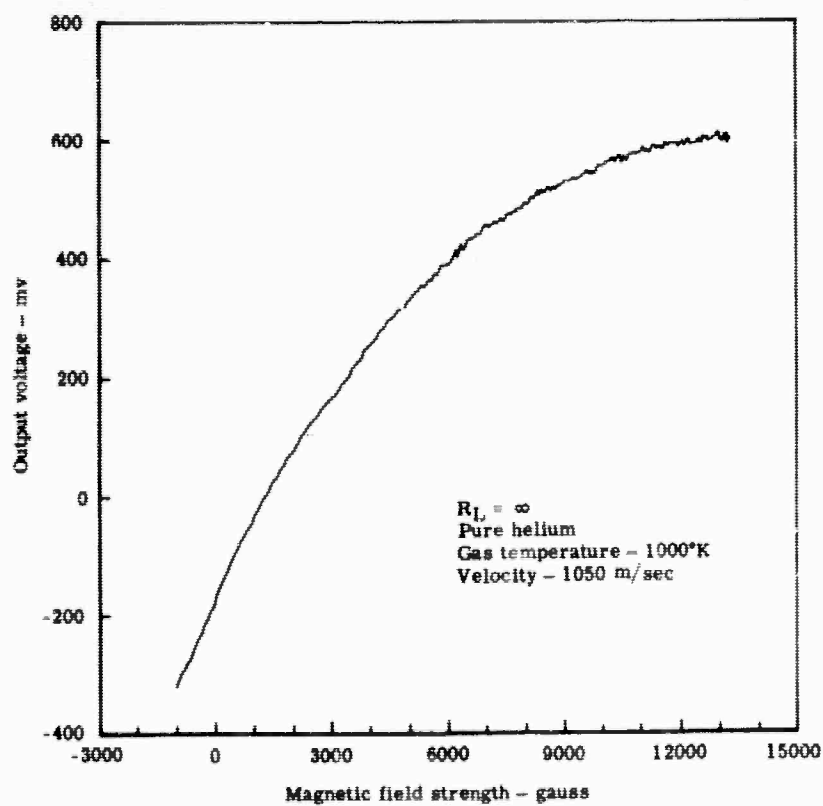
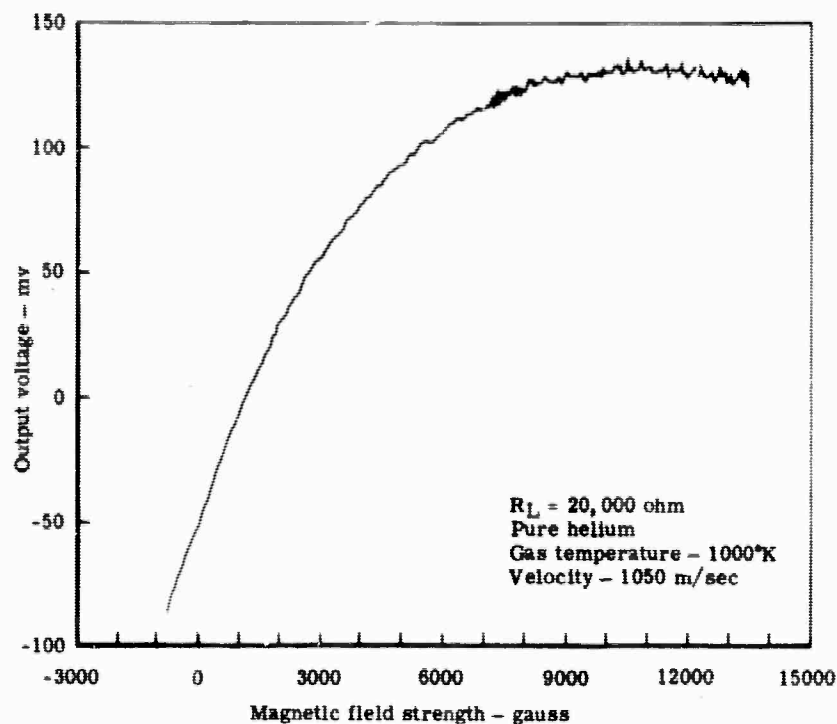


Figure 8. Voltage output recording without load.

## RUNS WITH HELIUM SEEDED WITH CESIUM

The analog instrumentation described previously was used to obtain both voltage-current and voltage output curves.

### Voltage-Current Curves

Figure 9 shows a family of voltage-current curves taken with different magnetic field strengths. The curves are nearly straight. Except for very low magnetic field strengths, the magnetic field seems to rotate the voltage-current curves around one point on the current axis. This can be explained as follows.

The voltage on a load resistor ( $V_L$ ) can be expressed as:

$$V_L = \left[ R_L / (R_I + R_L) \right] vBd \quad (1)$$

where

$R_L$  is the load resistor  
 $R_I$  is the internal resistance  
 $v$ ,  $d$ , and  $B$  are constants

The current is:

$$I = \left[ 1 / (R_I + R_L) \right] vBd \quad (2)$$

In the case of the voltage-current curves,  $v$ ,  $d$ , and  $R_I$  are constant and  $B$  is a parameter.  $R_I$  may be a function of  $B$ .

Equation (2) can also be written:

$$R_L = (vBd/I) - R_I \quad (3)$$

and therefore:

$$V_L = IR_L = vBd - IR_I \quad (4)$$



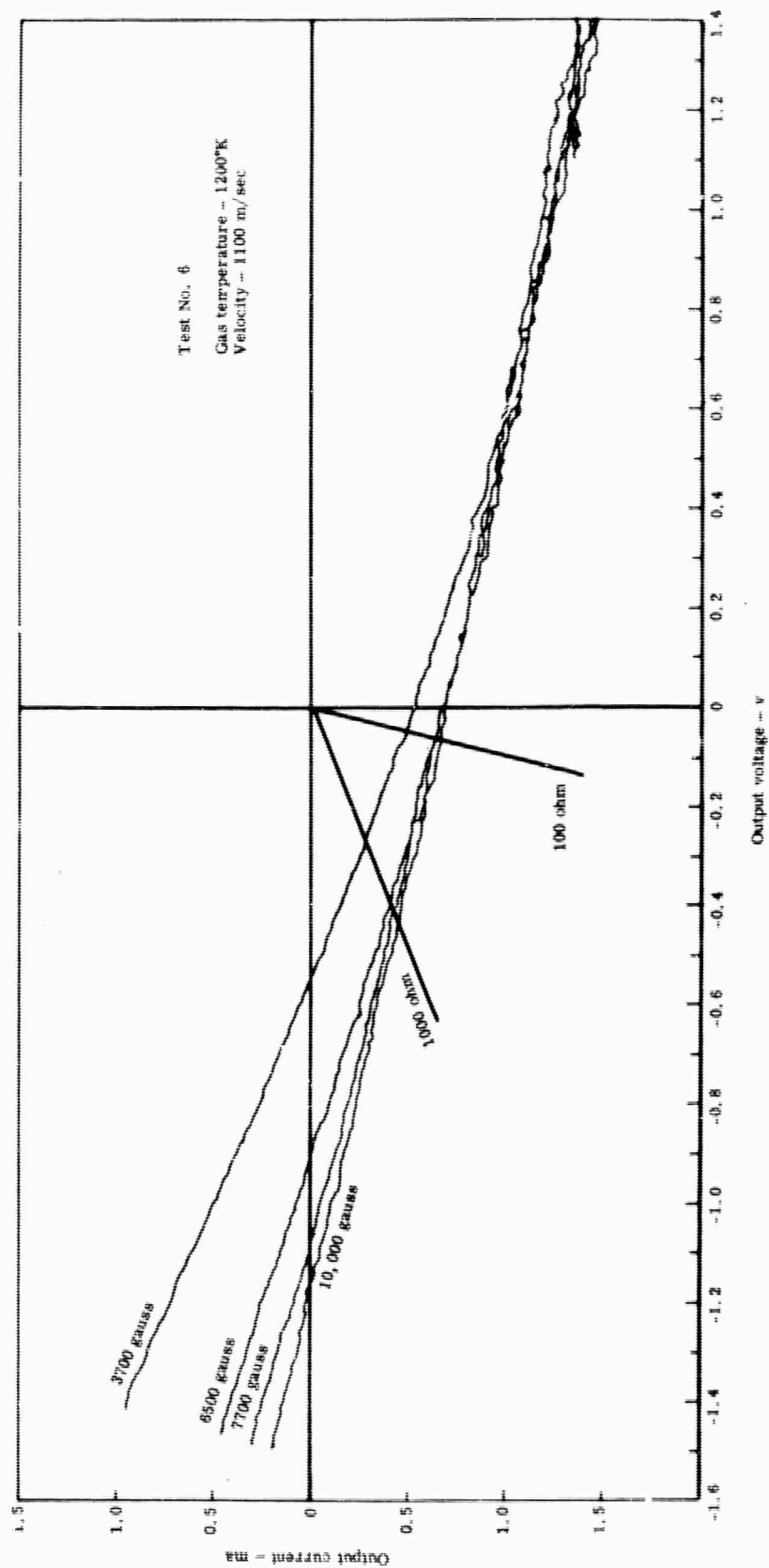


Figure 9. Voltage-current curves for cesium-seeded helium.

Now, assuming  $R_1 \sim \sqrt{1 + \omega^2 \tau^2}$  (as was explained previously\*), then for large values of  $\omega\tau$  and the following expression is obtained:

$$V_L \cong B(vd - CIR_{I0}) \quad (5)$$

where

$R_{I0}$  is the internal resistance without magnetic field

$C$  is a constant

Equation (5) shows that for large values of  $\omega\tau$ , the open circuit voltage is approximately proportional to the magnetic field while the short circuit current ( $V_L = 0$ ) does not depend on  $B$ . This explains the observed rotation of the I-V curves around one point at the short circuit current axis.

For small values of magnetic field, Equation (5) does not hold. If  $\omega\tau$  is in the order of unity, the short circuit current also depends slightly on the magnetic field, which can be easily seen when inserting  $R_1 = C_1 \sqrt{1 + \omega^2 \tau^2}$  in Equation (4):

$$I = vBd/C_2 R_{I0} \sqrt{1 + (e^2 B^2 \tau^2 / m^2)} \quad (6)$$

where  $C_2 = \text{constant}$

#### Voltage Output Curves

Figure 10 shows a family of voltage output curves for segmented electrodes, directly plotted with an x-y plotter. The character of the curves agrees with the curves previously reported.<sup>†</sup> The curves were taken with different load resistors to contrast with the previous data where only one load resistor was used. To compare the voltage-current and the voltage output curves, lines of constant resistance were drawn on the voltage-current curves. Transferring these points to the voltage output curves, on a line of constant field strength, showed that the points are very close to the actual recording.

---

\*Measurement of Fluid Properties for Magnetoplasmdynamic Power Generators—Fifth Quarterly Technical Summary Report (1 May—31 July 1964), Indianapolis, Indiana, Allison Division, GMC, EDR 3965, 17 August 1964, p 31.

<sup>†</sup>Ibid., p 30.

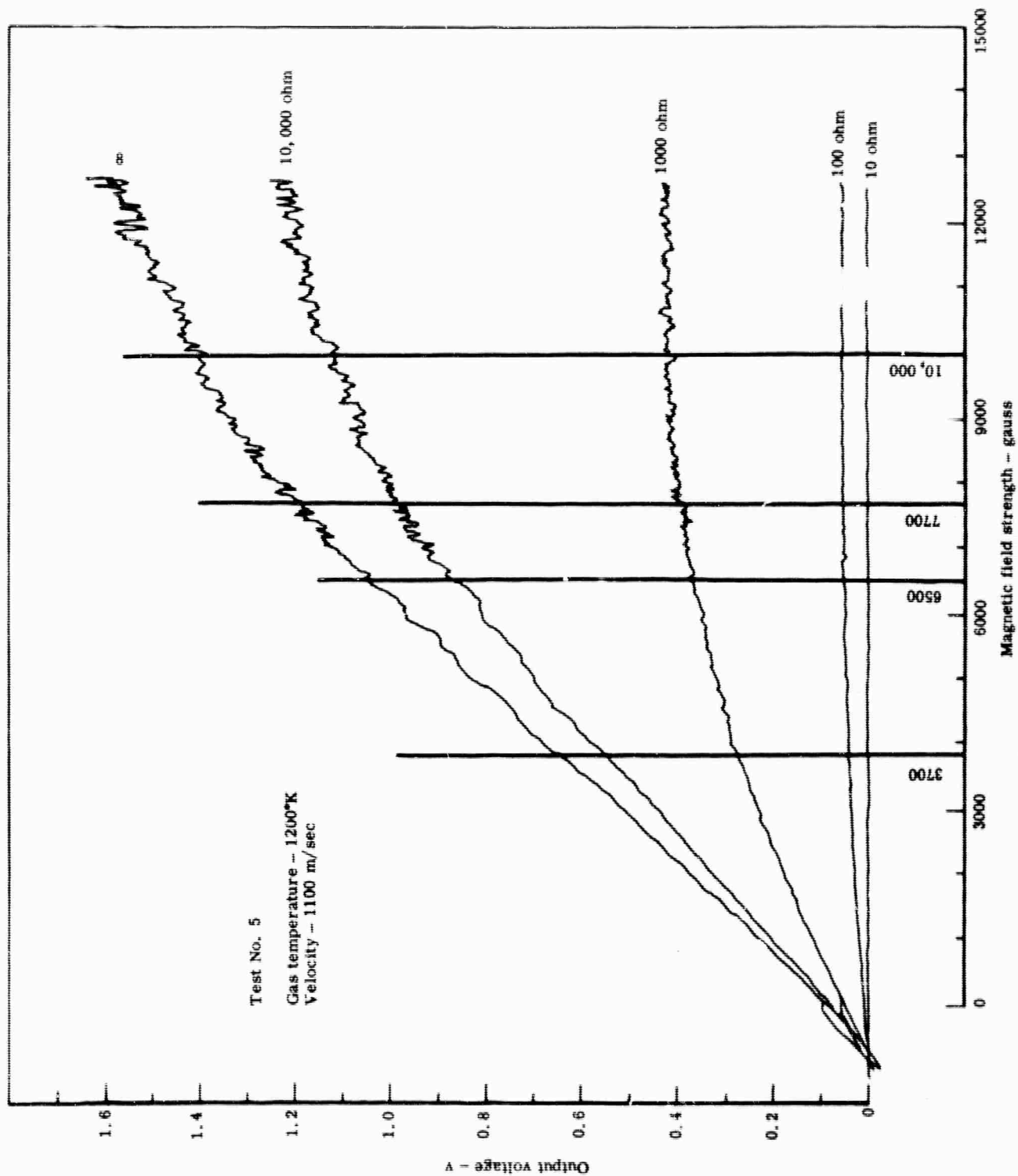


Figure 10. Voltage output curves obtained with segmented electrodes.

A possible explanation for the saturation effect was given previously.<sup>\*</sup> After runs have been made using the large test section now under construction, more information will be available to support or disprove this explanation.

#### SPECTROSCOPIC OBSERVATIONS

The primary problem associated with spectroscopic observations is the very weak intensity of the radiation of the helium-cesium mixture at approximately 1500°K. The intensities of the lines have been calculated and tabulated.<sup>†</sup> As has been demonstrated previously,<sup>‡</sup> the radiation of all lines is extremely weak at the temperature range under consideration. However, it was possible to detect a fairly large number of lines, within reasonable exposure times. The exposure time for the resonance lines was reduced to 5 sec. The exposure time for medium lines is approximately 1 min; weak lines require exposure times of 30 min or more.

The operation of the closed loop system is now reliable enough that constant gas temperature and constant cesium mass flow can be guaranteed much longer than 30 min. Those cesium and impurity lines which have been detected thus far are as follows:

<u>Cesium</u>	<u>Rubidium</u>	<u>Sodium</u>
8761Å	7947Å	8195Å
8521Å	7800Å	8184Å
8078Å		5890Å
7944Å		
6973Å		
4593Å		
4555Å		

To measure the absolute value of the electron temperature, both the line reversal method and the line ratio method have been used. To measure relative changes in electron temperature, the comparison of the intensity of the same line at different temperatures proved quite sensitive. This, of course, can be seen from the steep slopes of the curves shown previously.<sup>\*\*</sup>

<sup>\*</sup>Ibid., p 31.

<sup>†</sup>Measurement of Fluid Properties for Magnetoplasmadynamic Power Generators—First Quarterly Technical Summary Report (1 May—31 July 1963), Indianapolis, Indiana, Allison Division, GMC, EDR 3511, 20 August 1963, pp 45-58.

<sup>‡</sup>Ibid., Figure 19.

<sup>\*\*</sup>Ibid.

The line reversal method is well known and is often used especially when applied to the resonance lines of the alkali metals. The principal shortcoming of the line reversal method lies in the assumption that the temperature distribution is uniform within the plasma volume. If this is not true, then the errors introduced are difficult to correct.

Also, extreme care must be used when aligning the optical light path. Losses due to absorption in the windows and in colder gas regions in the light path may introduce errors. This method is quite sensitive to changes in temperature. It was possible to differentiate between two temperatures less than 50°K apart at the 1200°K level.

The absolute value of the temperature is relatively inaccurate, of course, because of the error introduced by losses due to absorption and the error in measuring the comparison blackbody temperature. By using very conservative estimates, however, the error in the temperature measured with this method cannot possibly be larger than  $\pm 75^\circ\text{K}$ .

Because of the question of temperature nonhomogeneity, line reversal was recorded photographically. Since temperature nonhomogeneity can now largely be disconnected, however, photoelectric recording is used, which makes routine measurements much easier and faster.

Figure 11 is a photograph of the reversal of the cesium resonance line approaching the reversal temperature at 1180°K. Figure 12 shows the densitometer traces of these photographs.

As a second method, the line ratio method was used. If a temperature profile exists, and if the plasma has cylindrical geometry, this method can be corrected by the Abel inversion. Here the line pair  $\lambda = 4555\text{\AA}$  and  $\lambda = 8078\text{\AA}$  was used. The results agreed with the results of the line reversal method within 10%. Of course, it is most desirable to use more than one line pair. To do this, the exposure times must be increased further. Runs of this type will be made in the near future.

Summarizing the spectroscopic temperature measurements to date, the electron temperature was always equal to the gas temperature, within the accuracy of measurement.

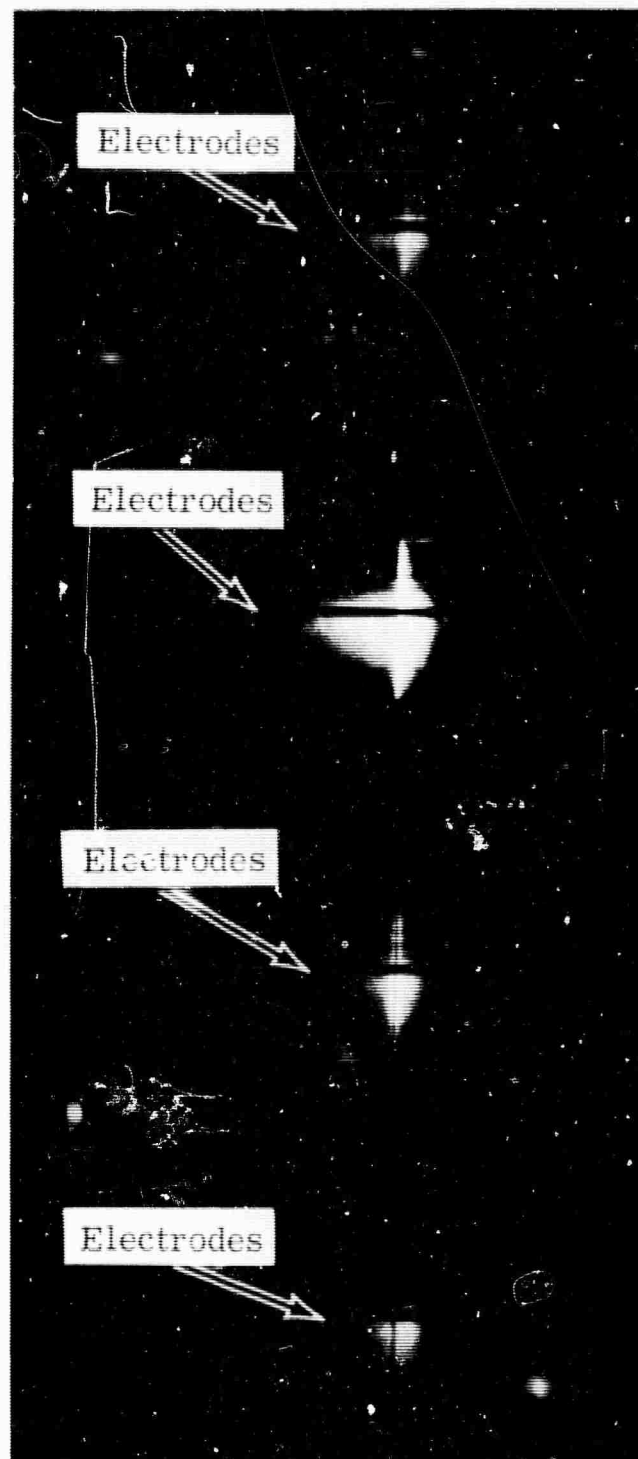


Figure 11. Spectrum photograph showing reversal of the cesium resonance line.

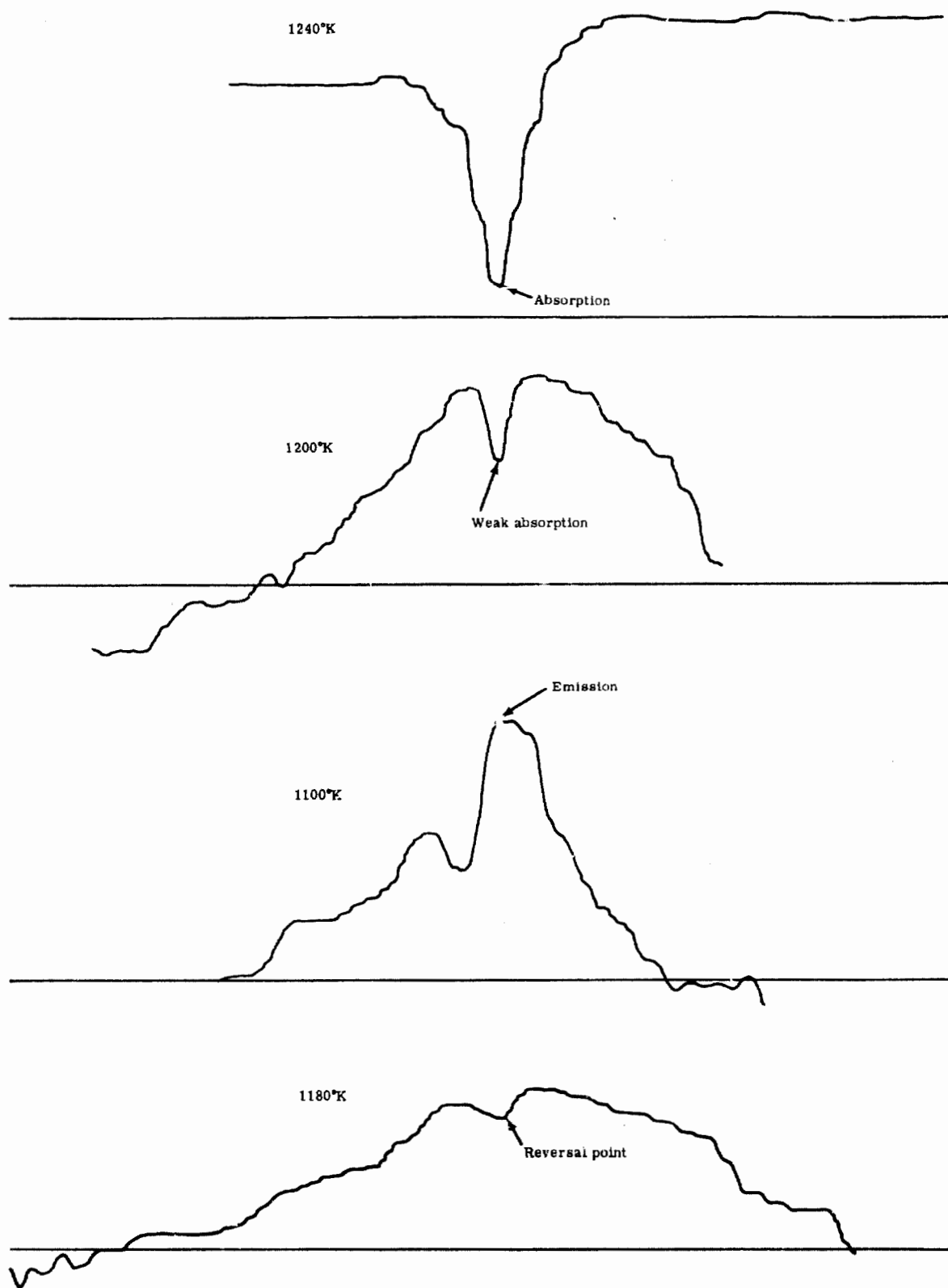


Figure 12. Densitometer traces showing reversal of the cesium resonance lines.

**BLANK PAGE**



#### IV. THEORETICAL INVESTIGATION

##### CALCULATION OF INTERCOMPONENT NONEQUILIBRIUM IN A MAGNETOPLASMADYNAMIC CONVERTER

###### Converter Model

The converter channel is assumed to be a rectangular duct of constant cross section as shown in Figure 13. The two horizontal duct walls are solid conductors and serve as electrodes. The electrodes are connected with a load,  $R$ . The magnetic field of constant induction,  $B_0$ , is applied perpendicular to the channel axis and coplanar to the electrode planes. The working fluid consists of four components—helium as carrier gas (o), cesium as seeding gas (a), and the ionization products of the latter, single cesium ions (i) and electrons (e).

###### Plasma Equations

For the theoretical description of the four-component flow, the multifluid equations for reacting plasmas based on the 13-moment approximation are used. These field equations have been given in detail\* and are not reviewed herein. To reduce the numerical effort, a few simplifications are made. Viscous effects and boundary layers are disregarded. The Hall effect is disregarded and the flow is treated as one-dimensional—i.e., all fields depend only on the coordinate in the direction of the channel axis. (Assume that the Hall effect is compensated

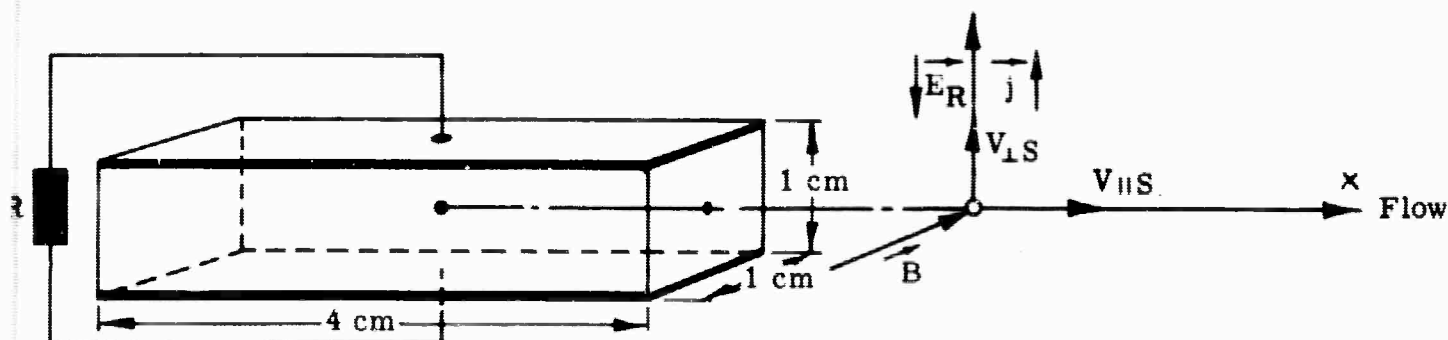


Figure 13. MPD converter cross section model.

\*Measurement of Fluid Properties for Magnetoplasmadynamic Power Generators—Third Quarterly Technical Summary Report (1 November 1963—31 January 1964), Indianapolis, Indiana, Allison Division, GMC, EDR 3743, 18 February 1964.

by some method.) Furthermore, energy losses due to heat conduction are not taken into account. Full consideration is given to (e-a) ionization and (e-i-e) recombination reactions, effects associated with the non-uniformity of the components, momentum transfer by intercomponent friction, and plasma heating by intercomponent friction.

## Initial Flow Data

Two converter flows, I and II, with different exterior loads,  $R$ , are considered. The exterior magnetic field,  $\vec{B}_0$ , is the same in both cases. Furthermore, at the channel entrance ( $x = 0$ ), the plasma pressure,  $P$ , temperature,  $T$ , Mach number,  $M$ , and particle composition are the same. The ionization at the channel entrance is calculated in accordance with the Saha equation.

The strong temperature-dependent Gvosdover cross sections ( $Q_{ei} = Q_{ie}$ ) are calculated in the program. The cross sections for neutral-neutral ( $Q_{ao} = Q_{oa}$ ) and neutral-charged ( $Q_{so} = Q_{os}$  and  $Q_{sa} = Q_{as}$ , where  $s = e, i$ ) particle interactions (rigid sphere model) are shown with elementary particle constants in Table I.

The characteristic quantities of the flow at the channel entrance are listed in Table II.

Table I. \*

### Elementary particle constants.

$Q_{eo} = 5.5 \times 10^{-16} \text{ cm}^2$	$m_o = 6.540 \times 10^{-24} \text{ gm}$
$Q_{ea} = 4 \times 10^{-14} \text{ cm}^2$	$m_a = 2.172 \times 10^{-22} \text{ gm}$
$Q_{io} = 9 \times 10^{-16} \text{ cm}^2$	$m_i = 2.172 \times 10^{-22} \text{ gm}$
$Q_{ia} = 2 \times 10^{-14} \text{ cm}^2$	$m_e = 9.108 \times 10^{-28} \text{ gm}$
$\epsilon_a = 3.893 \text{ ev}$	$e = 4.803 \times 10^{-10} \text{ esu}$

Table II.

### Initial flow values.

Plasma pressure, $P = 1.5 \times 10^6 \text{ dynes/cm}^2$	Plasma temperature, $T_o = 2000^\circ\text{K}$
Flow velocity, $v = 1.847 \times 10^5 \text{ cm/sec}$	Mach number, $M = 0.8$
Magnetic induction, $B_o = 18,000 \text{ gauss}$	Seeding ratio, $\alpha = 10^{-2}$
Helium density, $n_o = 5.38 \times 10^{18} \text{ cm}^{-3}$	Cesium density, $n_a = 5.38 \times 10^{16} \text{ cm}^{-3}$
Electron density, $n_e = 4.24 \times 10^{13} \text{ cm}^{-3}$	Ion density, $n_i = 4.24 \times 10^{13} \text{ cm}^{-3}$
Flow I— $R = 2.0 \text{ ohm}$	Flow II— $R = 6.6 \text{ ohm}$

\*S. C. Brown, Basic Data of Plasma Physics, J. Wiley and Sons, 1959.

## Results and Discussion

With respect to converter constants, the flows I and II differ only in the magnitude of the load ( $R_I < R_{II}$ ). This has, however, considerable consequences for the flow properties above the channel entrance, where  $x > 0$ . The load voltage is given by  $U = [R/(R_I + R)] vBd$ , where  $R_I$  is the interior resistance of the duct. Consequently, the field impressed by the load into the plasma ( $E = -U/d$ ) is smaller for flow I than for flow II with respect to the modulus ( $|E_I| < |E_{II}|$ ). Since the effective field acting on the electron component is

$$\vec{E}_1 = \vec{E} + \vec{v} \times \vec{B}_0 d \quad (7)$$

It is to be expected that flow I would exhibit stronger nonequilibrium effects than flow II. Figure 14 shows the main results of the numerical integration—the dependence of the electron temperature ( $T_e$ ) and the electron density ( $n_e$ ) on the flow coordinate ( $x$ ). For comparison purposes, the gas temperature field,  $T_0$ , is also given. The remaining fields of the heavy particle components, which did not change appreciably, are not shown. In accordance with the qualitative considerations, the exact numerical calculations indicate a more than twice as strong thermal nonequilibrium,  $|T_e - T_0| \neq 0$ , for flow I than for flow II. From Figure 14, the characteristic length after which the electron temperature is built up is read as:

$$\begin{aligned} \text{Flow I: } l_T &= 1.1 \times 10^{-2} \text{ cm} \\ \text{Flow II: } l_T &= 1.4 \times 10^{-2} \text{ cm} \end{aligned}$$

According to a previous analytical investigation, <sup>\*</sup>  $l_T$  is approximately given by:

$$l_T = v/(16/3) \sqrt{2kT_e/\pi m_e} \sum_r (m_e/m_r)(n_r Q_r) \quad (8)$$

Because of the predominating (e-o) interaction, it follows, using the constants from Tables I and II, that:

$$\begin{aligned} l_T &\approx v/(16/3) \sqrt{2kT_e/\pi m_e} (m_e/m_o)(n_o Q_{eo}) \\ &= (2.2)(10^{-2}) \sqrt{T_o/T_e} \text{ cm} \end{aligned} \quad (9)$$

---

\*assuming  $n_e \ll n_o$  and where ( $r = o, a, i$ )

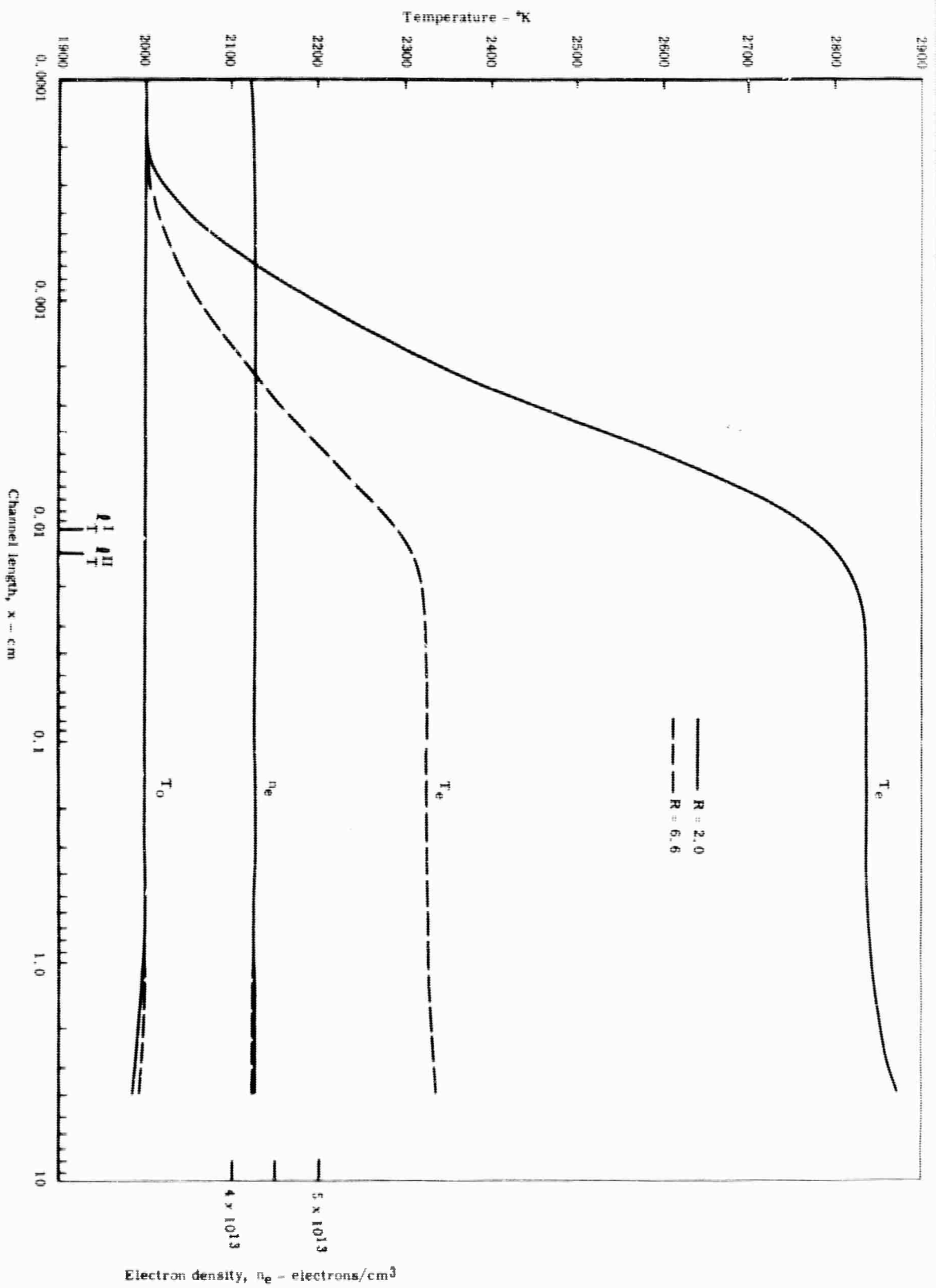


Figure 14. Results of numerical integration.

As the electron temperature changes considerably as  $x$  varies between zero and  $\ell_T$ , it is plausible to insert a mean value defined by  $\bar{T}_e = (1/2)(T_0 + \hat{T}_e)$ , where  $\hat{T}_e$  is the electron temperature at  $x = \ell_T$ , into Equation (9). With this correction, the agreement with the numerical calculations becomes fairly good.

From Figure 14, the full nonequilibrium electron temperature is read as:

Flow I:  $T_e = 2846^\circ\text{K}$

Flow II:  $T_e = 2325^\circ\text{K}$

Compare these values again with the simple analytical theory\* according to which

$$T_e/T_0 = 1 + (\mathcal{E}_1/E_f)^2 \quad (10)$$

The critical plasma field for frictional electron heating is given by:

$$E_f = \left\{ (1/e) \sqrt{3 \left[ \sum_{r \neq e} (m_e/m_r)(n_r Q_{er}) / \sum_{r \neq e} n_r Q_{er} \right] m_e k T_0} \right\} \nu_e \quad (11)$$

where the electron collision frequency ( $\nu_e$ ) is:

$$\nu_e \equiv (8/3) \sqrt{2 k T_e / \pi m_e} \sum_{r \neq e} n_r Q_{er} \quad (12)$$

Because of the predominating (e-o) interaction,  $E_f$  becomes, with the constants from Table II:

$$\begin{aligned} E_f &\approx (8/e) \sqrt{(2/3\pi)(m_e/m_o)(T_e/T_0) Q_{eo} n_o k T_0} \\ &= 22.37 \sqrt{T_e/T_0} \quad \text{v/cm} \end{aligned} \quad (13)$$

According to Equation (10), the field  $\mathcal{E}_1$  required for the production of an electron temperature  $T_e^I = 2846^\circ\text{K}$  and  $T_e^{II} = 2325^\circ\text{K}$ , respectively, is  $\mathcal{E}_1^I = 14.53 \sqrt{T_e/T_0}$  and  $\mathcal{E}_1^{II} = 9.05 \sqrt{T_e/T_0}$  v/cm, respectively. These values again agree satisfactorily with the results obtained numerically.

---

\*Measurement of Fluid Properties for Magnetoplasmadynamic Power Generators, Fourth Quarterly Technical Summary Report (1 February—30 April 1964), Indianapolis, Indiana, Allison Division, GMC, EDR 3861, 19 May 1964.

Figure 14 does not indicate a noticeable change in electron density,  $n_e$ . It can be shown that the characteristic length,  $l_p$ , required to build up the electron density corresponding to the elevated electron temperature, is large compared to the channel length. The low electron density explains the low values of the generated power for the two flow examples (see Table III).

Table III.  
Electrical flow quantities.

	<u>Load, R (ohm)</u>	<u>Current (amp)</u>	<u>Power (w)</u>
Flow I	2.0	4.90	48.98
Flow II	6.6	3.03	60.53

## Further Investigation

These preliminary calculations will be followed by computation for larger converter models for which the build-up of the electron density can be observed and a noticeable deceleration of the flow. Furthermore, it is intended to include additional physical effects which may be of importance for the nonequilibrium aspects of converter flows.

## ON THE NONOBSERVABILITY OF THE FULL OPEN FARADAY CIRCUIT VOLTAGE

The open load voltage of an ideal Faraday converter is  $U_1^G = \int_0^a v B_0 dx_1$  ( $v$  = flow velocity,  $B_0$  = magnetic induction,  $d$  = electrode distance). In actual experiment, in general, an open load voltage  $U_1 < \int_0^a v B_0 dx_1$  is observed. In the following, it is shown that this can be explained by Hall currents closed by leakage resistances. Other influential effects may still exist, however.

For Hall coefficients  $\omega\tau = (\sigma/n_e c) B_0 \gtrsim 1$ , the Hall effect is no longer negligible in plasma. In this case, Ohm's law assumes the form:

$$\vec{j} + \omega\tau \vec{j} \times (\vec{B}_0/B_0) = \sigma (\vec{E} + \vec{v} \times \vec{B}_0) \quad (14)$$

It follows for the current density parallel to the flow ( $\parallel$ ) and for the current density perpendicular to the flow and magnetic field ( $\perp$ ):

$$\vec{j}_{\parallel} = \left[ \sigma / (1 + \omega^2 \tau^2) \right] \left[ \vec{E}_{\parallel} + \omega \tau \vec{\nabla} B_0 - \omega \tau \vec{E}_{\perp} \times (\vec{B}_0 / B_0) \right] \quad (15)$$

$$\vec{j}_{\perp} = \left[ \sigma / (1 + \omega^2 \tau^2) \right] \left[ \vec{E}_{\perp} + \vec{\nabla} \times \vec{B}_0 - \omega \tau \vec{E}_{\parallel} \times (\vec{B}_0 / B_0) \right] \quad (16)$$

To measure the open load voltage of the Faraday converter, the Faraday load,  $R_{\perp}$ , is removed and replaced by a high impedance voltmeter. According to Equation (15), the instrument should indicate the voltage ( $\vec{j}_{\perp} = 0$ ):

$$U_{\perp} = - \int_0^d \vec{E}_{\perp} \cdot d\vec{x}_{\perp} \quad (17)$$

where

$$-\vec{E}_{\perp} = \vec{\nabla} \times \vec{B}_0 - \omega \tau \vec{E}_{\parallel} \times (\vec{B}_0 / B_0) \quad (18)$$

The field  $\vec{E}_{\parallel}$  is impressed on the plasma by a leakage resistance.

After elimination of  $\vec{E}_{\parallel}$  by means of Equation (15), Equation (18) becomes:

$$-\vec{E}_{\perp} = \vec{\nabla} \times \vec{B}_0 - (\omega \tau / \sigma) \vec{j}_{\parallel} \times (\vec{B}_0 / B_0) \quad (19)$$

Equations (18) and (19) show that in the presence of the Hall effect, the ideal Faraday field,  $-\vec{E}_{\perp}^0 = \vec{\nabla} \times \vec{B}_0$ , is diminished by a field  $-\vec{E}_H = -\omega \tau \vec{E}_{\parallel} \times (\vec{B}_0 / B_0) = -(\omega \tau / \sigma) \vec{j}_{\parallel} \times (\vec{B}_0 / B_0)$  which is induced by the flow of the Hall current across the magnetic field. Substitution of Equation (19) into Equation (17) finally gives the open Faraday load voltage in the form ( $b$  = duct width):

$$U_{\perp} = U_{\perp}^0 - (\omega \tau / \sigma b) I_{\parallel} \quad (20)$$

where

$$\text{Ideal open-load voltage: } U_{\perp}^0 = \int_0^d v B dx_{\perp} \quad (21)$$

$$\text{Hall current: } I_{\parallel} = b \int_0^d j_{\parallel} dx_{\perp} \quad (22)$$

Because  $\omega\tau/\sigma = B_0/n_e e$ , the observed open load voltage,  $U_1$ , should decrease as the electron density,  $n_e$ , decreases (at low temperatures) and increase as the magnetic field,  $B_0$ , increases. To experimentally prove Equation (19), the Hall leakage current,  $I_H$ , must be measured. A comparison of this preliminary theory with experiment will be presented in the final report.



## V. CONCLUSIONS

### SYSTEM DESIGN

The major problems in the design of a magnetoplasmadynamic system have been those associated with the gas heater, cesium seeding, helium purification, and helium-cesium separation. These problems have now been solved to the degree that reliable operation of the MPD system has been achieved.

### GENERATOR DESIGN

Operation of the present small MPD system yielded sufficient information to permit design of the large test section which is now under construction. Ceramic and tantalum parts were never subject to severe attack by cesium. The quartz window in contact with the hot cesium-helium mixture was found to devitrify immediately. No attack occurred, however, when the windows were sufficiently cooled. It was necessary, therefore, to remove the windows from direct contact with the hot working fluid.

### ELECTRON HEATING EFFECT

As previously mentioned, no increase in electron density is expected in the 4-cm channel (see Figure 14). Therefore, the usefulness of the electron heating effect can not be determined before the 50-cm channel is in operation.

As preliminary indications, however, the following observations can be reported. It was not possible to observe an increased electron temperature with load resistance down to 100 ohm. Since the measurements reported in previous quarterly summary reports were made, the numerical results represented in Figure 14 became available. From these results it can be seen that an increased electron temperature can hardly be expected when using a load even as low as 100 ohm. Attempts are being made now to detect this effect when running with short-circuit loads.